Laboratory adaptive optics system for testing the wave front sensor for the new MMT

T. A. Rhoadarmer[a], P. C. McGuire[b], J. M. Hughes[b], M. Lloyd-Hart[b],
J. R. P. Angel[b], S. Schaller[b], M. A. Kenworthy[b]

[a]US Air Force Research Laboratory, AFRL/DES, Kirtland AFB, NM 87117-5776 USA
[b]Steward Observatory, The University of Arizona, Tucson, AZ 85721 USA

ABSTRACT

A laboratory adaptive optics system has been built for testing the wave front sensor hardware and software for the new Multiple Mirror Telescope adaptive optics system. The system also allows different wave front reconstruction and prediction schemes to be examined. The laboratory system contains a silicon micromachined adaptive mirror with 37 electro-static actuators as well as a novel approach for generating atmospheric turbulence. The design and initial testing of the system are presented.

Keywords: adaptive optics, wave front sensors, deformable mirrors, generating turbulence, Kolmogorov phase plates

1. INTRODUCTION

The adaptive optics (AO) system for the new 6.5 m Multiple Mirror Telescope (MMT) has many complex elements.[1,2] Before the system can be installed on the telescope later this year, it is necessary for the various components to be fully tested and verified in the laboratory. This way, many of the problems associated with assembling and integrating a system of this complexity can be diagnosed and corrected without wasting valuable telescope time.

To this end, a small-scale laboratory AO system was built as a testbed for the MMT wave front sensor (WFS) hardware and AO control software. This test system was built as a precursor to a second, larger test facility which allows full-scale testing of the entire MMT AO system.[3,4] Besides the WFS for the MMT, the major components of the smaller laboratory system were a 37-actuator, micromachined deformable mirror (DM) and a set of static phase plates which generate Kolmogorov turbulence. The name for the test system, T37, was derived from the number of DM actuators. Descriptions of T37's major components and the design of the laboratory AO system are given below. Results from some initial system tests are also given.

2. SYSTEM COMPONENTS

2.1. Wave Front Sensor

The AO system for the MMT uses a Shack-Hartmann WFS to measure the phase aberrations of the incoming wave front. Its two main components are a low-noise, fast-readout CCD camera and a square-subaperture lenslet array. The camera for the WFS is a CCD39a device manufactured by EEV.[5] The detector is a thinned, back-illuminated device with a square 80×80 array format and $24 \ \mu m \times 24 \ \mu m$ pixels. The active area is 100% and the quantum efficiency in the visible is greater than 80%. The 4-port, split-frame transfer architecture has been optimized for high frame rates, up to 1 kHz if pixel binning is applied, and low read noise, from 3 to 6 electrons when operated at $-70°C$. The lenslet array was manufactured by Adaptive Optics Associates (AOA) and consists of a 50×50 square array of epoxy lenses stamped from a precise master and mounted on one side of a 6 mm thick, BK7 glass substrate. The lenses have a focal length of about 3.4 mm and a pitch of 144 μm.

The CCD and lenslet were custom built so the pitch of the lenslet array was an integer multiple of the CCD pixel size—one subaperture lens is commensurate with a 6×6 subarray of CCD pixels. This feature made it possible to permanently fix the registration of the lenslet to the CCD by precisely aligning the components and bonding them together with epoxy. This design avoids the use of reimaging optics between the lenslet and CCD and eliminates the

---

Other author information:
T.A.R.: Email: rhoadart@plk.af.mil, Telephone: 505-846-5022
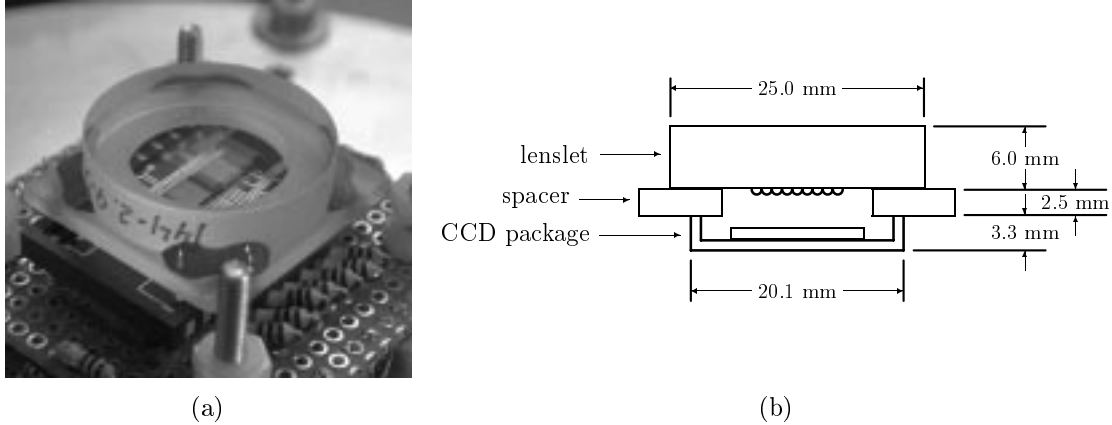P.C.M.: Email: mcguire@as.arizona.edu, Telephone: 520-621-7870

Figure 1. The WFS after the lenslet has been bonded to the CCD package. Figure (a) shows the WFS after assembly. Figure (b) displays a cross sectional diagram the WFS. A spacer of BK7 glass, machined to the appropriate thickness, was used to create a one focal length separation between the lenslet array and the CCD detector plane.
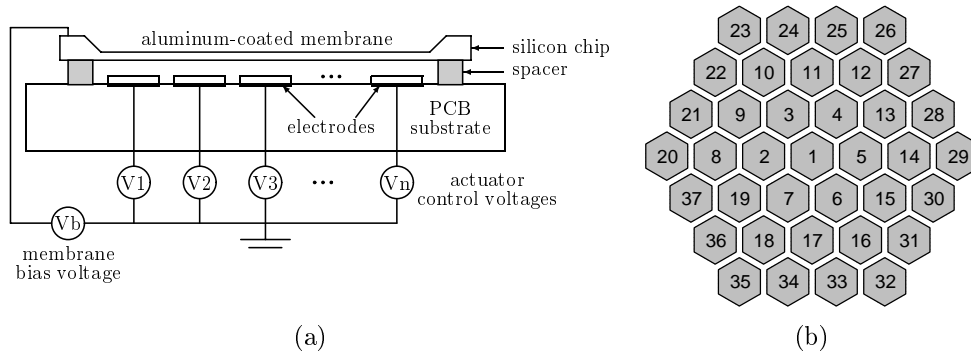

Figure 2. OKO adaptive mirror. Figure (a) shows a schematic of the cross-section of the mirror. Figure (b) shows the layout of the hexagonal-shaped actuators.

hassle of having to realign the WFS registration during experiments. To our knowledge, constructing a WFS in this fashion has never before been accomplished.

For the first generation of the MMT AO system, the WFS geometry consists of a 12 × 12 array of square subapertures. Figure 1 shows an image of the assembled WFS. A description of the process used to assemble the WFS is given in [6]. The registration between the lenslet array and CCD is quite good. Under normal illumination, with an unaberrated, collimated beam, the average offset of the focused spots from their respective quad cell centers is less than 1 μm and the maximum offset is less than 2.5 μm.

2.2. Deformable Mirror

The DM for the T37 system was manufactured by OKO Technologies. It was a micromachined adaptive mirror with integrated, electro-static actuators.[7,8] The mirror was fabricated using silicon bulk micromachining technology, making it relatively inexpensive. In addition, the entire system, mirror and control electronics, consumed only 10 W of power. A simplified schematic of the adaptive mirror is shown in figure 2.[†] This DM was designed for correcting low order aberrations.[8] Since atmospheric turbulence is dominated by the lower order modes, this DM was expected to perform well in the T37 system.

The reflective surface of the DM, a thin membrane of aluminum-coated silicon nitride, had a clear aperture of about 15 mm. The membrane was suspended about 100 μm above an array of 37 electrodes and was only supported along its circular outer boundary. The electrodes were individually addressable and served as the actuators. The layout for the hexagonal-shaped electrodes is also shown in figure 2. This configuration is similar to the DM for the

---

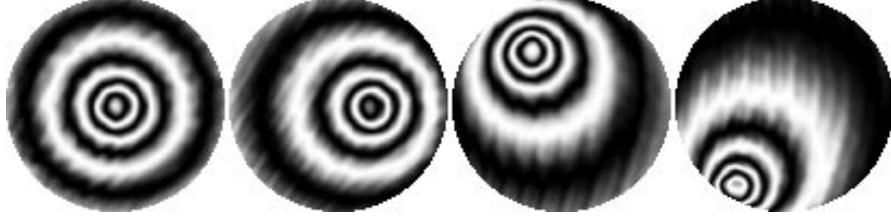[†]Figure diagrams used with permission from G. Vdovin, OKO Technologies, 1998.

Figure 3. Sample actuator influence functions. Synthetic interferograms of the influence functions for actuators 1, 5, 10, and 35 are shown from left to right for DAC inputs of 255. The interferograms show the central 12 mm of the mirror surface in double-pass at a wavelength of 0.6328 μm.

MMT AO system. The center-to-center spacing of the electrodes was 1.75 mm. The center electrode was roughly centered within the clear aperture of the mirror and the entire actuator structure fit within a 12 mm circle.

By applying voltages to the actuator electrodes, the mirror surface could be deflected toward the electrodes by electro-static attraction. The magnitude of this force was given by

$$F = \frac{\varepsilon_0 V_c^2 S}{d^2}, \tag{1}$$

where F is the force, ε_0 is the dielectric constant of air, which was the intermediate medium, V_c is the control voltage, S is the surface area of the electrode, and d is the separation distance. To correct for positive and negative wave front aberrations, a bias was applied to the actuators to set the nominal operating position of the mirror halfway between the undeflected, zero-voltage surface and the surface of maximum deflection. The maximum allowed deflection of the DM center was specified at about 9.5 μm. Therefore, the nominal operating position of the mirror was chosen to have a 4.75 μm center deflection, which corresponds to a radius of curvature of about 6 m.

A computer was used to control the voltages applied to the DM actuators. Each of the 37 output channels were controlled by a separate low-voltage, digital-to-analog converter (DAC). High-voltage DC amplifiers were then used to amplify the DAC outputs to the operational range required by the DM, 0–190 V. The DACs had 8-bit resolution and their outputs were trimmed so that any set of actuator control values could be sent to the mirror without fear of damaging it. Because the mirror response was proportional to the square of the actuator voltages, the uniform DAC input value for the mirror's nominal operating position was 180 ($\approx 255/\sqrt{2}$). While these electronics could operate at more than 1 kHz, the mechanical settling time of the DM membrane was about 1 ms. Therefore, the maximum update rate for the T37 system was limited to about 500 Hz since it was desired that the mirror figure be stable during WFS integration.

Although an extensive model of the DM had already been developed, the mirror needed to be characterized for use with the T37 system.[7] This characterization required the measurement of the actuator influence functions. To measure the influence function of each actuator, the DAC inputs for all the actuators were set to zero, except for the actuator of interest whose DAC value was stepped uniformly in force from 0 to 255. Interferometric surface measurements for all actuators were made at DAC settings of 0, 128, 180, 221, and 255. These settings corresponded to approximately 0%, 25%, 50%, 75%, and 100% of the maximum actuator force. Surface data were collected at additional DAC settings for selected actuators. Influence functions for four of the actuators are shown in figure 3. Because these actuators are force actuators, as compared to position actuators such as piezo-electric stacks, the influence functions are non-local and very broad in extent. On the other hand, unlike piezo-electric actuators, these actuators do not exhibit any hysterisis.[8]

Besides providing information for developing reconstruction algorithms for the T37 AO system, the data collected in this experiment were used to verify several aspects of the mirror's structure and operation. The amount of actuator misalignment was characterized by finding the minimum of the influence function for each actuator. Figure 4 shows the results of the actuator misalignment study. The rms offset between the expected and measured actuator locations is 0.13 mm, or about 7.5% of the actuator spacing.

The variation in actuator stroke and the relationship between influence function amplitude and control voltage were also examined. Figure 5(a) shows the max-min deviation of the 37 actuator influence functions for different DAC inputs. The four curves in the figure correspond to uniform force increments of the actuator control voltages, from 0 to 100%. These data show the region of the mirror surrounding actuator 13 has a much weaker response to the actuator control voltages. The voltages at the mirror were measured to be uniform to within 2% when a uniform
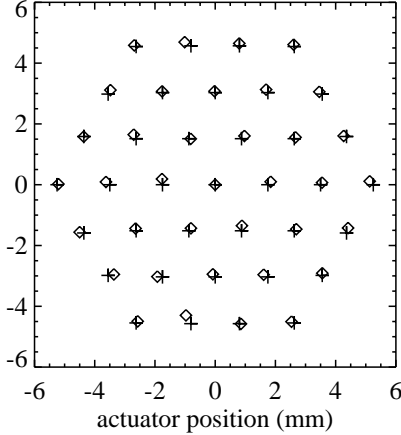
Figure 4. Locations of the OKO adaptive mirror actuators. The "+" signs mark the expected locations of the actuator centers and the "◇" symbols mark the positions of the actuator centers determined from the influence function minimums.
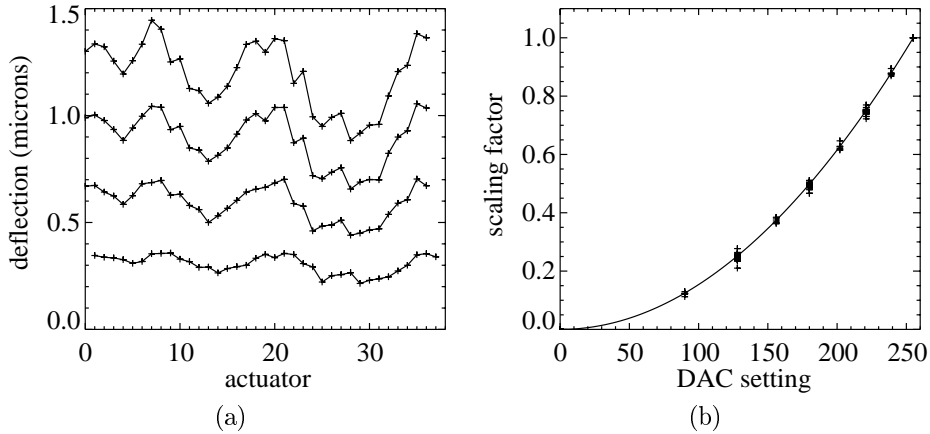

(a)

(b)

Figure 5. Actuator dynamic range analysis for the OKO adaptive mirror. Figure (a) shows the variation in actuator stroke across the mirror. From bottom to top, the curves correspond to a DAC input of 128, 180, 221, and 255. Figure (b) demonstrates the square-law relationship between actuator deflection and DAC input value. The "+" signs denote the calculated scaling factors and the solid curve is the expected square-law.

DAC setting was applied to all of the actuators. Therefore, it appears either the mirror was stiffer in this region or the membrane-to-actuator distance was greater.

The deflection of the mirror surface was expected to be proportional to the applied actuator force.[7] With that thought in mind, equation 1 pointed to a square-law relationship between surface deflection and actuator control voltage. The data shown in figure 5(a) seemed to substantiate this opinion. The validity of this assumption was tested by calculating each actuator's influence function scale as a function of DAC setting. The results of the analysis are shown in figure 5(b). The scaling factors were determined by minimizing the rms difference between an actuator's influence function for a DAC input value of 255 and that same actuator's influence function for other DAC settings. By definition, the scaling factor is exactly 1.0 for a DAC input value of 255. Tilt removed influence functions were used for this calculation. The figure shows the square-law relationship holds true.

A minor drawback of the OKO DM is that it is a nonlinear device. When multiple actuators are poked at the same time, the resulting mirror deflection does not equal the sum of the individual pokes. Table 1 and figure 6 demonstrate this nonlinearity. The major difference between the interferogram pairs shown in the figure is not in the shape, but in the magnitude of the deflection. This characteristic is typical of this type of membrane-actuator system. As equation 1 shows, the actuator force is inversely proportional to the square of the membrane-electrode separation. For the OKO mirror, the membrane-electrode separation could change by as much as 9.5 μm out of roughly 100 μm, or about 10%. Therefore, the nonlinearity from this effect alone could reach 20%. Another cause of the nonlinearity may have been cross-talk between actuators. There appears to be some evidence of this effect in the interferograms

scenario	actuator	DAC	scale
1	2–7	180	1.11
2	10	221	1.37
	14	180	
	18	128	
3	1,5	180	1.43
4	2	128	1.20
	17	221	
	36	180	

Table 1. Simultaneous, multiple actuator poke scenarios. Columns 2 and 3 list the actuators that were simultaneously activated and their DAC commands. All other actuators had DAC commands of zero. The last column lists the scale factor that must be applied to the individual-poke sum in order to minimize the rms difference between it and the actual measured surface.
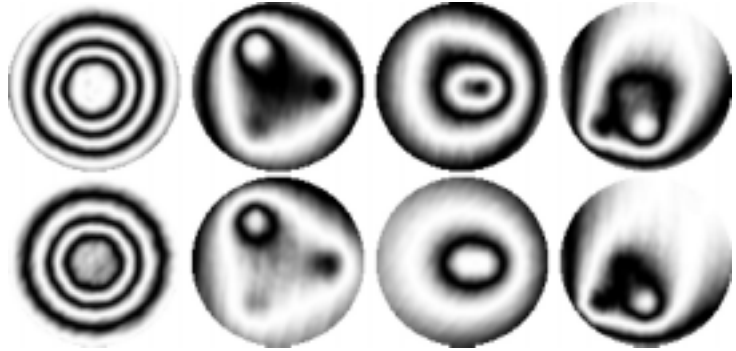

Figure 6. Comparison of simultaneous, multiple actuator pokes to the sum of the individual pokes. The synthetic interferograms in the top row are the measured surface deflections for the scenarios described in table 1. The interferograms on the bottom are the surfaces calculated by summing the corresponding individual actuator pokes. Global tilt has been removed in each case. The scenarios are shown from left to right. The interferograms show the central 12 mm of the mirror surface in double-pass at a wavelength of 0.6328 μm.

for scenarios 3 and 4. The additional structure seen in the measured surfaces for these scenarios indicates additional actuators may have been active. Fortunately, the nonlinearities were small for small perturbations of the actuator control voltages and linear control still produced good results in a closed-loop system like T37.

2.3. Kolmogorov Phase Plates

A set of static phase plates which generate Kolmogorov turbulence were created in order to perform tests with the T37 system in the presence of atmospheric-like turbulence. Unlike turbulence generator assemblies (TGA) which rely on the forced motion of hot air, static phase plates allow for more controlled testing of an AO system.[9,10] Most importantly, the exact shape of the phase aberrations induced by the plates can be independently measured. In addition, the speed and amplitude of the turbulence can be independently controlled and multiple tests can be run multiple times with the same "turbulence sequence."

The design of the static-phase-plate TGA had three requirements. First, the temporal and spatial statistics had to be controllable and similar to the statistics observed at the MMT facility on Mt. Hopkins. Second, the TGA had to operate over a broad range of wavelengths so that the distortion incurred at all wavelengths matched in optical path difference (OPD), in microns not waves, to the extent it would after propagation through the atmosphere. Third, the TGA will eventually be integrated into the instrumentation box on the MMT telescope for *in situ* testing. This prospect limits the size of the assembly as well as the mechanical and electrical resources which are available for operating the TGA.

There are a number of techniques which can be used to manufacture static phase plates. These include binary diffractive optics, plastic mold optics, computer generated holography, and nearly index-matched (NIM) optics.[11,12] The major drawback of the first two options is the cost. In comparison, computer generated holography is potentially the cheapest approach if film is used instead of a CGH writer. However, the wavelength dependence of a hologram is quite different from the atmosphere. After taking into consideration cost and wavelength dependence, index matching was chosen as the best approach.

The design of our turbulence phase plates is demonstrated in figure 7. A Kolmogorov phase profile, defined by $f(\mathbf{x})$, where $\mathbf{x}$ is a 2-dimensional position vector, was machined into the surface of a substrate of optical quality acrylic. Clear mineral oil which had an index close to the index of the acrylic was then sandwiched between the substrate and a second acrylic window as shown in the figure. The OPD for rays passing through this assembly is given by

$$
\begin{aligned}
\text{OPD}(\mathbf{x}) &= (n_2 - n_1)(f(\mathbf{x}) - \overline{f}), \\
&= \Delta n \, \Delta f(\mathbf{x}),
\end{aligned}
\tag{2}
$$

where n_1 and n_2 are the refractive indices of the materials and $\overline{f}$ is the average deviation of the interface. Any beam of light which passes through the NIM sandwich will have a copy of the interface function imprinted on its phase.
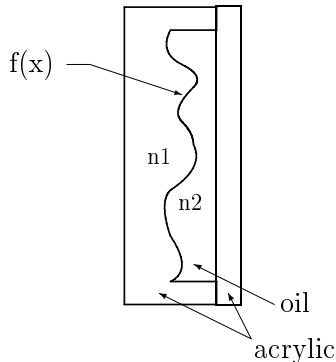

Figure 7. Diagram of an nearly index-matched phase plate.

Wave fronts aberrated by atmospheric turbulence have an OPD peak-to-valley of only a few microns. This scale of OPD variation can be produced with good resolution by choosing materials for which Δn is small, on the order of 0.01. The actual physical deviation of the profile machined into the acrylic substrate could then be several hundred microns. Commercial-grade milling machines can produce surface variations of this scale with a height resolution of 5–10 μm, making it possible to manufacture NIM sandwiches at a reasonable cost. Compared to binary optics, the transverse resolution is much larger, about 250 μm, but atmospheric wave front aberrations are composed mainly of low spatial frequencies, so this transverse resolution should be fine as long as the diameter of the optical beam passing through the plate is not too small.

A small prototype phase plate was made to test the design concept described above.[13] Acrylic ($n = 1.491$) was used as the substrate material because of its homogeneity and machinability. After some experimentation, a white, heavy mineral oil was found which had an index very close to acrylic ($n = 1.482$).[‡] Using a computer numerical control (CNC) milling machine, a 2 inch × 2 inch Kolmogorov surface, with a sample spacing of 0.01 inches, was machined into a 3/8 inch thick, acrylic substrate using a 1/16 inch ball endmill. The amplitude of the machined surface was chosen so the resulting phase profile imprinted on an optical beam had a Fried coherence length, r_0, of 1.0 mm in the visible. This surface was covered with mineral oil and a 1/4 inch thick plate of acrylic was used for the opposing window. This NIM sandwich was bolted together and the interface between the acrylic plates was sealed with tape.

A Mach-Zender interferometer was used to measure the prototype phase plate. A comparison between the target and measured turbulence profiles is given in figure 8. The two phase profiles match very well. The major differences between them mainly consist of large scale variations. These differences may have been caused by thermal expansion of the acrylic or the milling machine during machining, a calibration error in the milling machine, or variations in the thickness or refractive index of the acrylic material. Whatever the reason, it is of little concern since the resulting phase profile is still pseudo-random and it exhibits Kolmogorov statistics of the proper magnitude. In fact, the variations were such that the actual surface matched better to the theoretical model than the target surface did.

After the success with the prototype, a set of 8 inch diameter phase plates were made. For each of these plates, mineral oil was sandwiched between two 1/4 inch thick, circular acrylic disks. The phase profile was machined into one of these disks with an amplitude designed to produce turbulence with an r_0 of 1.4 mm in the visible. This r_0 was chosen so the turbulence imprinted on a diverging beam passing through two of these plates would simulate the seeing conditions at the MMT. The phase profile was contained within a 2.25 inch wide annular region which could be rotated through the T37 optical beam by a motor to simulate dynamic turbulence. A picture of one of these plates is shown in figure 9 along with its target phase profile. As seen in the figure, several bolts were used to hold the plates together and two o-rings, one outside the turbulence ring and one inside, were used to seal the oil between the plates. In addition, a rotation axis was attached to the phase plate through a hole in the plate's center.

Due to the potential presence of wedge in the acrylic plates, two modes of tilt were subtracted from the phase profiles before machining. First, global tilt was removed by subtracting the best fit plane to the annular phase region. This procedure was done so the amount of tilt in the optical beam would be less likely to oscillate wildly as the phase plate rotated though it. Second, in order for the average amount of tilt imprinted on the beam to be zero, a radial tilt mode was also removed. This mode was defined as $T_{rad}(\mathbf{r}) = c \, r$, where $\mathbf{r}$ is a two-dimensional position vector with magnitude r whose origin is the axis of rotation and c is the amplitude of the tilt mode.

After assembling the first plate, a simple test was performed to characterize the turbulence produced by it. For this test, specklegrams were recorded using different regions of the phase plate. A 21 mm diameter, collimated laser

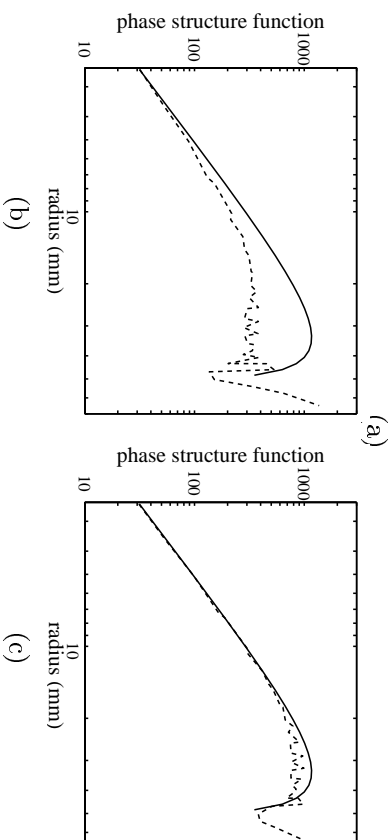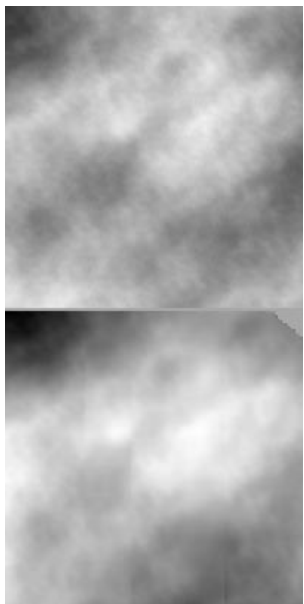‡Paraffin oil, liquid petrolatum, Mallinckrodt Specialty Chemicals Company, lot #6357.

(b)

(a)

Figure 8. Target and measured turbulence phase profiles for the small prototype oil-filled phase plate. Figure (a) shows images of the target surface on the left and of the measured surface on the right. Overall tilt has been removed from both images. Figures (b) and (c) show the phase structure functions for the target and measured surfaces, respectively. The solid curves on these graphs denote the tilt-removed Kolmogorov structure function for the designed r_0 of 1.0 mm.

phase structure function

10

radius (mm)

10   100   1000

(a)

phase structure function

10

radius (mm)

10   100   1000

(c)
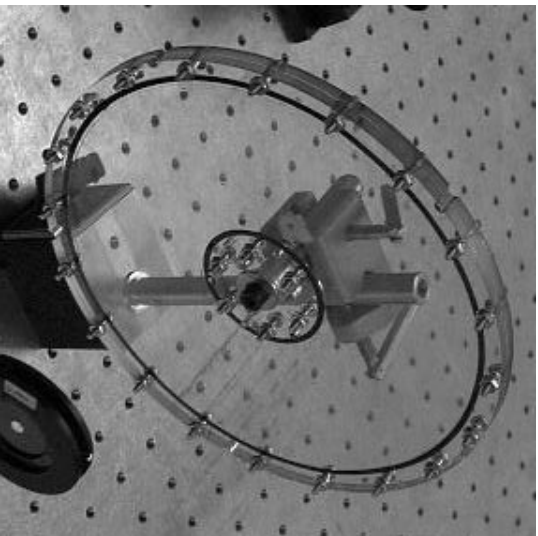
(a)

(b)

Figure 9. Picture of the 8 inch oil filled phase plate. Figure (a) shows the phase plate mounted on the test stand used during initial testing of the plate. Figure (b) shows the target phase profile for the prototype polymer-filled phase plate. The inner and outer radii for the phase profile are 1.28 inches and 3.53 inches, respectively.
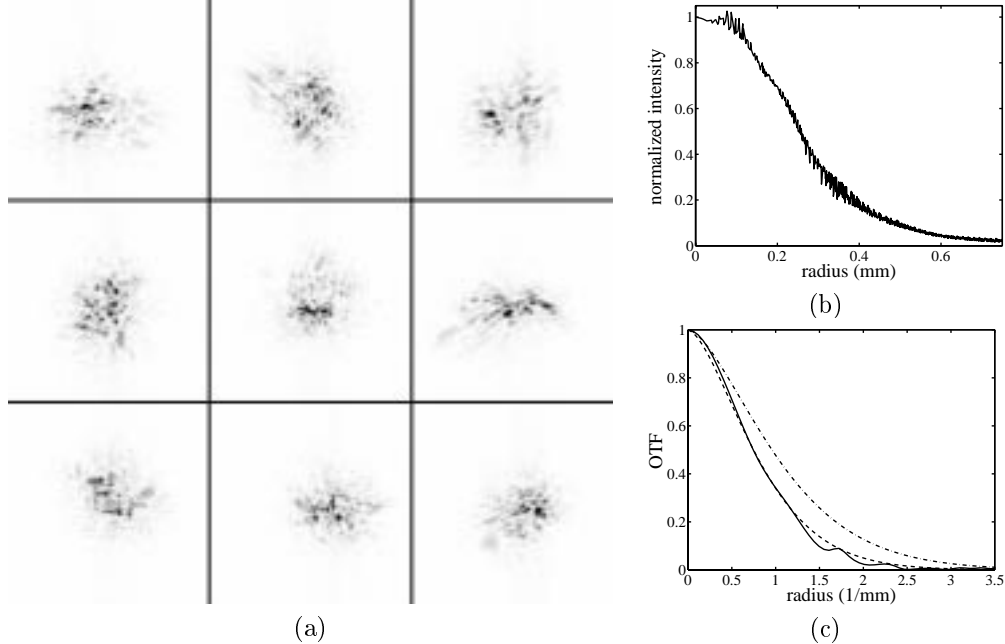
Figure 10. Analysis of the 8 inch oil-filled phase plate. Figure (a) shows a series of specklegrams recorded from different regions of the plate. Figures (b) and (c) show radial profiles of the estimated short-exposure image and OTF, respectively. The dash-dot and dashed curves in figure (c) correspond to the theoretical, tilt-removed OTFs for the target r_0 value of 1.4 mm and the measured r_0 value of 1.12 mm, respectively.

beam was passed through the plate and then focused onto a camera by an optical system which had a focal length of 1110 mm. Figure 10 shows the set of images that were recorded. Using these data, an estimate of the average short-exposure image was obtained by shifting and adding the specklegrams. During the shifting process, the image centroids were determined by calculating the first moment of the intensity profiles. Using the average image, the tilt-removed OTF was calculated.[14,15] The result of this calculation is also shown in the figure. From the e^{-1} point of the OTF, the value of r_0 was estimated at 1.12 mm. Theoretical OTFs, for this estimate of r_0 and the target value of 1.4 mm, are shown as well. Based on the estimate of r_0, the turbulence was slightly stronger than expected, but it was not too far from the target value. The discrepancy could easily be due to the fact that only a few images were used to estimate the structure function.

The phase plates will be used for simulating dynamic turbulence during laboratory testing of the MMT AO system. The strength of the turbulence produced by the plates will be controlled by placing them in a diverging beam. By sliding the plate along the axis of the beam, the value of D/r_0, where D is the diameter of the beam, can be varied over a wide range.[14,16] In addition, the speed of the turbulence can be varied by controlling the rate at which the plates are rotated. Lastly, by using multiple phase plates in the system, multiple atmospheric layers can be simulated and longer, non-repeating "turbulence sequences" can be created.

3. SYSTEM DESIGN

A diagram of the T37 system is shown in figure 11. The system had five major sections—the laser source, the global tilt mirror (GTM), the DM, the WFS, and the imaging camera. Optical relay systems connected these elements together to create a working AO system.

A 5 mW HeNe laser was used as the illuminating source for the system. The beam from the laser was spatially filtered and collimated by lens $L1$ before it reached the entrance aperture of the imaging system. The entrance aperture was defined by a 24 mm variable aperture. A set of neutral density filters ($ND1$), placed before the spatial filter, allowed the intensity of the beam to be adjusted to proper levels for the WFS and imaging cameras.

The output from the WFS was used to control two adaptive mirrors. The OKO DM was used to correct the residual wave front errors after overall tip-tilt was corrected by the GTM. The GTM was a necessary addition to the system because using the DM to correct for full-aperture tilt would have limited the actuator stroke available
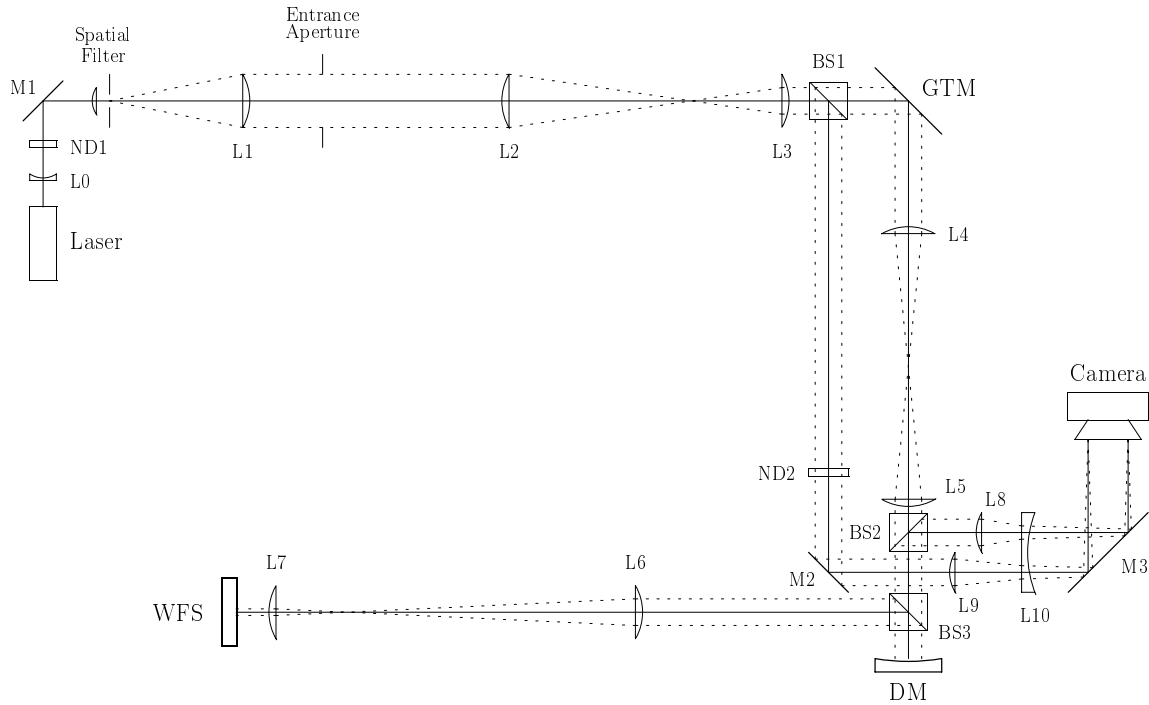
Figure 11. Diagram of the T37 laboratory AO system.

for higher-order aberration correction. All three of these components, WFS, DM, and GTM, were located at pupils of the system. The WFS and DM were operated at normal incidence, but the GTM was operated at a nominal incidence angle of 45 degrees.

Three optical relay systems, of two lenses each, were used to image the entrance aperture onto the GTM, DM, and WFS. The first relay system, $L2$ and $L3$, was an afocal system which imaged the aperture onto the GTM with a magnification of 0.445. The next relay system, $L4$ and $L5$, was composed of two identical lenses which produced a one-to-one imaging system between the GTM and the DM. This system was not quite afocal, but presented a wave front to the DM which matched the mirror's 6 m nominal radius of curvature. The last relay system, $L6$ and $L7$, imaged the DM onto the WFS lenslet array with a magnification of 0.108. Overall, with the DM at its nominal position, the entire system, from $L1$ to $L7$, was afocal with a magnification of 0.048.

With the entrance aperture diameter set to 21 mm, the beam size on the DM was 9.35 mm so the actuators extended slightly outside the beam. Having the size of the beam smaller than the extent of the actuators allowed reasonable aberration control over the entire aperture and reduced the influence of the fixed membrane boundary. In addition, this entrance pupil diameter mapped nicely onto a 7×7 block of subapertures on the WFS. By ignoring the 3 subapertures in each corner which were less than 50% illuminated, 37 active WFS subapertures remained. This geometry produced an overdetermined system with twice as many slope measurements (74) as actuators (37), resulting in good noise reduction and system stability. A diagram of the AO geometry is shown in figure 12.

The imaging system was designed so both the open-loop and closed-loop images could be placed on the same camera with the same scale. Beamsplitter $BS1$ picked off the open-loop wave front before the GTM and $BS2$ picked off the closed-loop wave front after it returned from the DM . The neutral density filter $ND2$ was used to attenuate the open-loop wave front so its intensity could be more closely matched to the closed-loop wave front. Lenses $L8$ and $L9$ were identical positive lenses which focused the closed-loop and open-loop beams, respectively, onto the same focal plane. Separate lenses were needed because the closed-loop wave front was converging while the open-loop wave front was collimated. The location of the final focal plane of the imaging system was determined by the negative lens $L10$. By moving this lens with respect to the two lenses preceding it, effective focal lengths from 0.5 m to more than 10 m could be created. This design made it possible to scale the resulting images so their diffraction limit was several pixels in diameter and reasonable sampling was achieved.

Since all of the lenses in the system were operating on-axis at greater than $f/16$, and since achromatic doublets were used at the critical points, the aberrations introduced by the relay lenses were small. Unfortunately, the
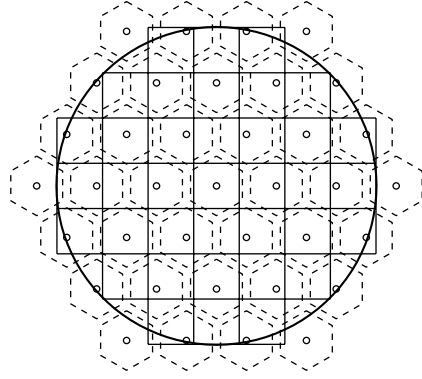
Figure 12. Geometry of the T37 laboratory AO system. The DM actuators and WFS subapertures have been projected onto the entrance pupil. The large circle represents a 21 mm entrance pupil diameter. The hexagons are the DM actuators and the squares are the WFS subapertures. The small circles mark the centers of the actuators.
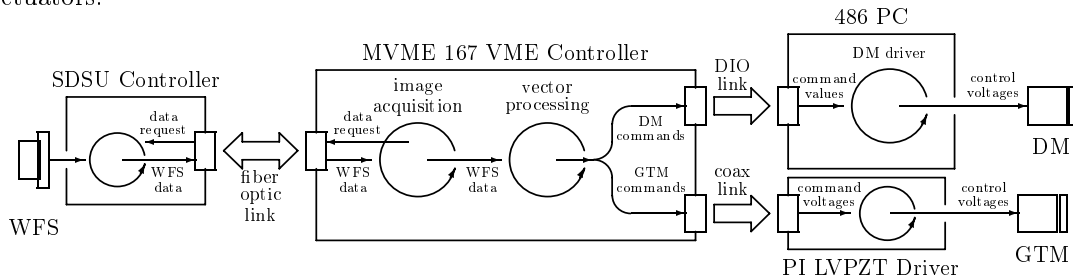

Figure 13. Diagram of the hardware and software control system for the T37 AO components.

beamsplitters were another story. These elements were stock items and the surface flatness over their one inch clear apertures was only guaranteed to $\lambda/2$ at 0.6328 μm. In the T37 system, the beam size at the cubes was less than 11 mm so the effective flatness was probably better than $\lambda/2$. However, multiple cubes were used in the system, so the cumulative effect was significant.

A diagram of the hardware and software that controlled the T37 AO components is shown in figure 13. Two computers were used in the control system. The main computer was a VME system running VxWorks. The VME was used to initialize and interface with the WFS Leach/SDSU controller through a fiber optic link. This hardware and software interface was similar to the one that will be used at the MMT, so the rest of the T37 system was built around it.

The interface for the DM required a 486 PC running DOS since the computer interface cards that controlled the mirror were made for a PC. This PC was connected to the VME through digital input-output ports. Due to the speed of this connection, the VME acted as the main processing and control unit and the PC simply served as a relay box for the DM commands.

The GTM was a Physik Instruments (PI) 2-axis, fast steering mirror with an angular resolution of 1 μrad and a range of about $\pm$2 mrad. It was controlled by a PI low-voltage PZT driver connected by coax cables to two 16-bit, 10 V DACs located in the VME crate.

Closed-loop, linear control was used in the T37 system.[17,18] After capturing a WFS image, the VME adjusted the data for dark and flat field effects and calculated the subaperture slopes. The wave front was then reconstructed using a matrix-vector multiply. An updated set of actuator commands were determined from this wave front and output to the DM and GTM. A separate global tilt sensor was not used, so the actuator commands for the DM and GTM were both derived from the WFS data.

4. INITIAL SYSTEM TESTS

After fine tuning the system alignment and verifying the operation of the control hardware and software, it was time to close the AO loop and perform some initial tests. A least-squares reconstructor, based on the geometry of the
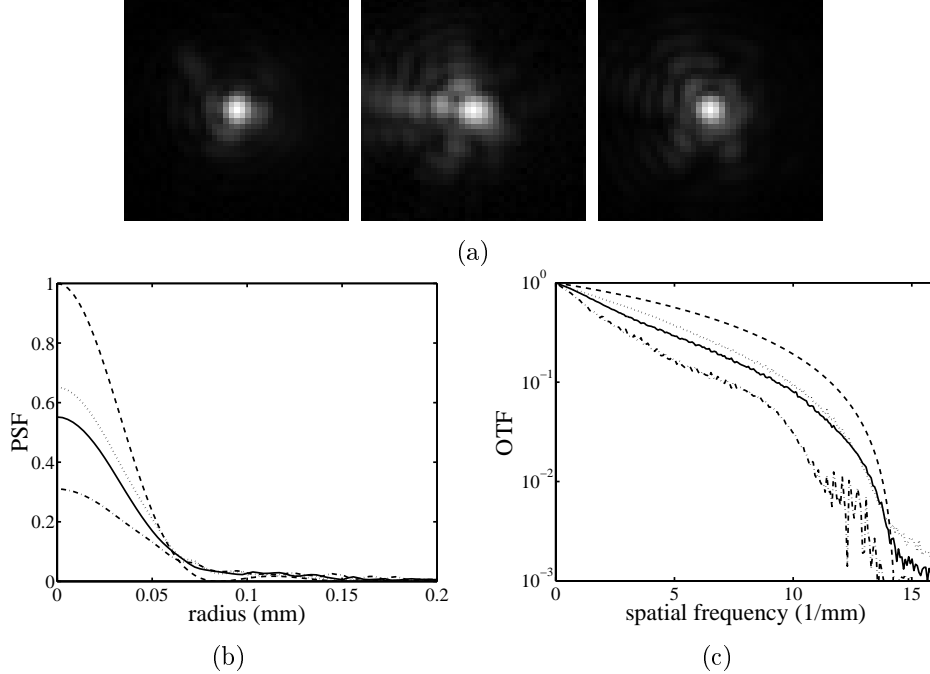
(a)

(b)   (c)

Figure 14. Images from closing the loop on the T37 system. From left to right figure (a) shows the open-loop, uncompensated closed-loop, and compensated closed-loop PSFs, respectively. The image fields are 0.98 mm across. In order to better show their structure, the square root of the PSF images is displayed. Figures (b) and (c) show the average radial PSFs and OTFs. The curves correspond to the uncompensated closed-loop PSF (dash-dot-dash), the compensated closed-loop PSF (solid), the open-loop PSF (dotted), and the theoretical diffraction limited PSF (dash-dash).

system, was created for this purpose. To account for any residual alignment errors between the DM and WFS, the system's geometry, or poke, matrix was experimentally determined. Once the reconstructor was created, the AO control loop was closed on the T37 system with an actuator update rate of about 5 Hz. Two tests were performed at this point. The results from these tests are presented below. During these tests the imaging system was configured at $f/110 \pm 1$.

For the first test, the AO loop was closed on the system only. The internal systematic aberrations, introduced by the various components, were the only thing considered. Figure 14 shows the recorded images from the open-loop and closed-loop light paths before and after closing the loop. The uncompensated closed-loop image was recorded after setting all of the DM actuator commands to their nominal value of 180. The average radial PSFs and OTFs are also shown in the figure. The open-loop PSF had a Strehl ratio of 0.65 ± 0.01 and the closed-loop PSF had a Strehl of 0.31 ± 0.01 before the control loop was closed, and 0.55 ± 0.01 after.

The improvement resulting from closing the control loop was quite good. However, the fact that the compensated closed-loop image was not as good as the open-loop image was disconcerting. There were two possible explanations for this result. First, the closed-loop light path had more components than the open-loop path and some of these components were not sensed by the WFS. Second, the DM may have been unable to correct the wave front any better. This explanation appeared plausible after comparing the expected and measured wave front errors. From computer simulations of Kolmogorov turbulence, the Strehl ratio of 0.55 for the compensated PSF indicated an rms wave front error of 0.86 radians.[13] This wave front error matched well to the wave front reconstructed from the residual WFS slopes which had an rms error of 0.73 radians. Furthermore, in similar closed-loop experiments performed by the manufacturers of the DM, wave front fitting errors on the order of 0.5–1.0 radians were reported.[8]

The second test performed with the AO system looked at the ability of the system to correct for static external turbulence. The small prototype phase plate described above was used for this experiment. The turbulence plate was in the optical beam about 25 mm after the pinhole of the spatial filter assembly. The plate was placed at this location so the amount of turbulence added to the beam was not excessively large. The beam diameter at the turbulence surface was 3.0 mm so D/r_0 was about 3. Lens $L1$ was adjusted to compensate for the defocus created
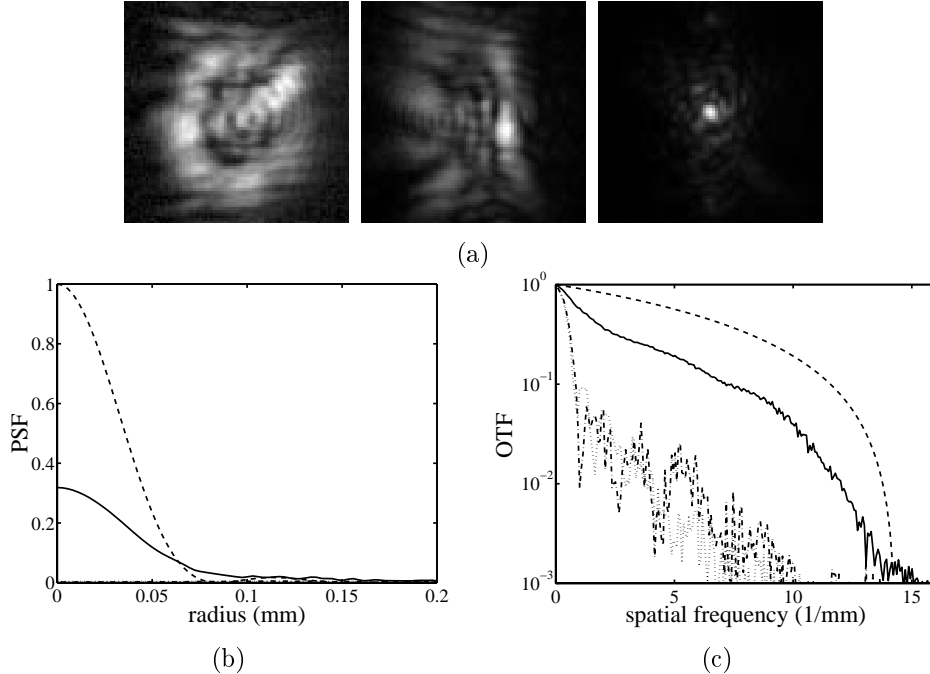
(a)

(b)   (c)

Figure 15. Images from closing the T37 loop on external turbulence. From left to right figure (a) shows the open-loop, uncompensated closed-loop, and compensated closed-loop PSFs, respectively. The image fields are 1.94 mm across. In order to better show their structure, the square root of the PSF images is displayed. Figures (b) and (c) show the average radial PSFs and OTFs. The curves correspond to the uncompensated closed-loop PSF (dash-dot-dash), the compensated closed-loop PSF (solid), the open-loop PSF (dotted), and the theoretical diffraction limited PSF (dash-dash).

by the thickness of the turbulence plate. Unfortunately, the mount which held $L1$ did not have enough range to completely remove the defocus.

Figure 15 shows the images recorded during the second test along with the average PSF and OTF radial profiles. The image fields in this figure are twice as big as those in figure 14. The open-loop PSF had a Strehl ratio of 0.012 ± 0.001. The closed-loop PSF had a Strehl of 0.040 ± 0.001 before closing the control loop, and 0.32 ± 0.01 after. The improvement resulting from closing the control loop is very good in this case. Most of the improvement is due to the fact that the wave front aberration is dominated by defocus and the DM is able to fit defocus fairly well.[8]

5. CLOSING COMMENTS

The T37 AO system has been used to perform initial testing and debugging of the hardware and software for the WFS for the new MMT. Currently, efforts are focused on closing the AO loop in the presence of dynamic turbulence. To accomplish this task, the speed of the calculation and application of the DM commands needs to be increased. The maximum actuator update rate is limited to 500 Hz because of the settling time of the DM.[8] However, at present, the interface between the VME and PC limits the update rate to a few tens of hertz.

In order to more accurately characterize the 8 inch turbulence plates, efforts are being made to obtain complete phase maps of the turbulence profiles, similar to the one shown in figure 8 for the 2 inch prototype. Work is also being done to build better phase plates. The major concerns with the oil-filled plates are the mismatch in dispersion and CTE between the oil and acrylic and the potential for oil leaking on neighboring optical components. The solution to both of these problems is to replace the mineral oil with an optical polymer. Potential polymers have been located and efforts are underway to refine the machining and assembly process.

After the MMT AO system comes online, the T37 system will be used for continued testing of wave front reconstruction algorithms. Of particular interest is the application of predictive techniques to compensate for the degradation in system performance resulting from the temporal delay required for the WFS integration and wave front reconstruction steps.[19,20]

REFERENCES

1. M. Lloyd-Hart, G. Angeli, R. Angel, P. McGuire, T. A. Rhoadarmer, and S. Miller, "Infrared adaptive optics system for the 6.5-m MMT: system status," in *Astronomy with Adaptive Optics – Present Results and Future Programs*, ESO Conf. Proc. , (European Southern Observatory, Garching, Germany), 1998.

2. G. Brusa and C. D. Vecchio, "Design of an adaptive secondary mirror: a global approach," Appl. Opt. **37**, pp. 4656–4662, 1998.

3. P. C. McGuire, M. Lloyd-Hart, J. R. P. Angel, G. Z. Angeli, R. L. Johnson, B. C. Fitz-Patrick, W. B. Davidson, R. J. Sarlot, C. J. Bresloff, J. M. Hughes, S. M. Miller, S. Schaller, F. P. Wildi, M. A. Kenworthy, R. M. Cordova, M. L. Rademacher, M. H. Rascon, J. H. Burge, B. L. Stamper, C. Zhao, P. Salinari, C. D. Vecchio, A. Riccardi, G. Brusa, R. Biasi, M. Andrighettoni, D. Gallieni, C. Franchini, D. G. Sandler, and T. K. Barrett, "Full-system laboratory testing of the F/15 deformable secondary mirror for the new MMT adaptive optics system," in *Adaptive Optics Systems and Technology*, R. K. Tyson and R. Q. Fugate, eds., Proc. SPIE **3762**, 1999.

4. R. Sarlot and J. Burge, "Optical system for closed-loop testing of adaptive optic convex mirror," in *Novel Optical Systems and Large-Aperture Imaging*, K. D. Bell, M. K. Powers, and J. M. Sasian, eds., Proc. SPIE **3430**, 1998.

5. B. Leckie and T. Hardy, "Gemini WFS CCDs and controllers," in *Optical Astronomical Instrumentation*, S. D'Odorico, ed., Proc. SPIE **3355**, pp. 529–538, 1998.

6. P. C. McGuire, T. A. Rhoadarmer, M. Lloyd-Hart, J. C. Shelton, J. R. P. Angel, G. Z. Angeli, J. M. Hughes, B. C. Fitz-Patrick, M. L. Rademacher, S. Schaller, M. A. Kenworthy, F. P. Wildi, J. G. Capara, M. P. Lesser, and D. B. Ouellette, "Construction and testing of the wavefront sensor camera for the new MMT adaptive optics system," in *Adaptive Optics Systems and Technology*, R. K. Tyson and R. Q. Fugate, eds., Proc. SPIE **3762**, 1999.

7. G. V. Vdovin, *Adaptive mirror micromachined in silicon*. PhD thesis, Delft University of Technology, 1996.

8. G. Vdovin, "Optimization-based operation of micromachined deformable mirrors," in *Adaptive Optical System Technologies*, D. Bonaccini and R. K. Tyson, eds., Proc. SPIE **3353**, pp. 902–909, 1998.

9. E. P. Magee and B. M. Welsh, "Characterization of laboratory-generated turbulence by optical phase measurements," Optical Eng. **33**, pp. 3810–3817, 1994.

10. D. S. Acton, P. L. Wizinowich, P. J. Stomski, J. C. Shelton, O. Lai, and J. M. Brase, "Laboratory calibration of the W. M. Keck Observatory adaptive optics facility," in *Adaptive Optical System Technologies*, D. Bonaccini and R. K. Tyson, eds., Proc. SPIE **3353**, pp. 125–131, 1998.

11. S. M. Ebstein, "Nearly index-matched optics for aspherical, diffractive, and achromatic-phase diffractive elements," Opt. Let. **21**, pp. 1454–1456, 1996.

12. M. Otsubo, H. Takami, and M. Iye, "Holographic atmospheric turbulence simulator for testing adaptive optics systems," Publ. Astro. Soc. Pac. **109**, pp. 1057–1061, 1997.

13. T. A. Rhoadarmer, *Construction and Testing of Components for the 6.5 m MMT Adaptive Optics System*. PhD thesis, University of Arizona, Optical Sciences Center, 1999.

14. D. L. Fried, "Optical resolution through a randomly inhomogenous medium for very long and very short exposures," J. Opt. Soc. Am. **56**, pp. 1372–1379, 1966.

15. A. C. Slavin, A. L. Wells, R. Q. Fugate, D. L. Fried, and J. J. Drexler, "A comparison of three methods of measuring the atmospheric coherence length," in *Propagation and Imaging through the Atmosphere*, L. R. Bissonnette and C. Dainty, eds., Proc. SPIE **3125**, pp. 241–249, 1997.

16. R. J. Noll, "Zernike ploynomials and atmospheric turbulence," J. Opt. Soc. Am. **66**, pp. 207–211, 1976.

17. B. L. Ellerbroek, "First-order performance evaluation of adaptive optics systems for atmospheric turbulence compensation in extended field-of-view telescopes," J. Opt. Soc. Am. A **11**, pp. 783–805, 1994.

18. W. J. Wild, "Innovative wavefront estimators for zonal adaptive optics systems," in *Adaptive Optics and Applications*, R. K. Tyson and R. Q. Fugate, eds., Proc. SPIE **3126**, pp. 278–287, 1997.

19. B. L. Ellerbroek and T. A. Rhoadarmer, "Real-time adaptive optimization of wave-front reconstruction algorithms for closed-loop adaptive-optical systems," in *Adaptive Optical System Technologies*, D. Bonaccini and R. K. Tyson, eds., Proc. SPIE **3353**, pp. 1174–1185, 1998.

20. P. C. McGuire, D. G. Sandler, M. Lloyd-Hart, and T. A. Rhoadarmer, *Scientific Applications of Neural Nets, Lecture Notes in Physics*, ch. Adaptive Optics: Neural Network Wavefront Sensing, Reconstruction, and Prediction. Springer, Heidelberg, 1999.